

Selective CO₂ to proportionally tunable syngas at lower onset potential enabled by bimetallic chalcogenides in polyoxometalate medium

Wencong Sun ^a, Li Zhou ^a, Wenzhe Tian ^a, Shumiao Li ^a, Min Yang ^b, Chunxiang Li ^{a,*}

^a Energy Chemical Engineering Professional Laboratory, School of Chemistry and Chemical Engineering, Harbin Institute of Technology, Harbin 150001, PR China

^b MIIT Key Laboratory of Critical Materials Technology for New Energy Conversion and Storage, School of Chemistry and Chemical Engineering, Harbin Institute of Technology, Harbin 150001, PR China



ARTICLE INFO

Keywords:
CO₂ reduction
Syngas
Bimetallic chalcogenides
Polyoxometalate
In situ surface-enhanced Raman spectroscopy

ABSTRACT

Highly active noble metals and developed modified electrocatalysts are limited in terms of economy and kinetics for the electrocatalytic CO₂ reduction reaction (ECO₂RR), respectively. Herein, different bimetallic chalcogenides (CuInSe₂, CuInS₂, AgInS₂) were found to have the ability to prepare proportionally tunable syngas in PV₃Mo₉ medium at an ultra-low onset potential of -0.1 V (vs. RHE). The ECO₂RR system established by CuInSe₂ and PV₃Mo₉ achieved the widest CO/H₂ range (1.0–5.1), with a maximum j_{CO} of -29.3 mA·cm⁻². The PV₃Mo₉ medium had a positive effect on reducing the onset potential and improving the reaction kinetics. Theoretical calculations illustrated that the high activity of CuInSe₂ in PV₃Mo₉ medium depended on the metal-like characteristic generated by the interaction of bimetallic orbitals and the mild regulation of *CO adsorption energy. This work demonstrates the broad application prospects of bimetallic chalcogenides in POM media in terms of ECO₂RR activity and economic benefits.

1. Introduction

As a mixture of CO and H₂, syngas is an important raw material for modern petroleum production [1]. It is well known that syngas mixtures with different CO/H₂ ratios can be used in different processes. For instance, syngas with a CO/H₂ ratio of 1:2 is widely used for Fischer Tropsch synthesis, while syngas with a CO/H₂ ratio of 1:1 (or with even higher CO content) is an important raw feedstock for alcohol production via carbonyl/hydroformylation and fermentation [2]. Currently, proportionally tunable syngas is usually prepared through coal gasification and natural gas reforming, which rely on non-renewable fossil fuels [3]. Thus, alternative and sustainable strategies for producing tunable syngas are urgently needed. Driven by renewable clean energy electricity, the highly controllable electrocatalytic CO₂ reduction reaction (ECO₂RR) coupled with water electrolysis can solve this issue and effectively achieve carbon neutrality [4,5].

A vast range of catalyst materials such as metals [6,7], heteroatom-doped carbon materials [8–10], and transition metal-organic frameworks [11,12] have been proposed to address the issues with ECO₂RR, which include low catalytic activity, high overpotentials, and uncontrollable selectivity. Nevertheless, simultaneously addressing these problems in a single catalytic system remains a notable

challenge. As an emerging type of catalytic material, transition metal chalcogenides (such as Ag₂S, SnO₂, MoS₂, and CuSe) possess many attractive physical and chemical properties, including unique d-orbital electronic configuration, superior conductivity at room temperature, and highly adjustable active sites [13–15]. Liu et al. decreased the onset overpotential to 54 mV (vs. RHE) over Ag₂S nanowire catalysts and achieved a current density 17.5 times higher than that of bulk Ag. They confirmed that the d-band center of the surface Ag atoms of Ag₂S (121) had higher d-electron densities than the surface Ag atoms of Ag (111), reducing the transition state energy of ECO₂RR [16]. However, bimetallic chalcogenides exhibit better electronic structures and improved electrocatalytic activity properties compared to monometallic chalcogenides. Wang et al. found that CoIn₂Se₄ displayed much higher activity than CoSe₂ and In₂Se₃ in water splitting, which was attributed to the combination of these two metals lowered the energy barrier for oxygen evolution [17]. Wang et al. also discovered that the ECO₂RR activity of v-CuInSe₂ was superior to that of In₂Se₃ and CuSe₂, as the interaction between the Cu and In orbitals induced a moderate adsorption strength for intermediates and favored the ECO₂RR pathway to CO, and the element composition of bimetallic chalcogenides plays a more critical role than crystal structure in determining ECO₂RR performance [18]. Accordingly, bimetallic chalcogenides are considered highly promising

* Corresponding author.

E-mail address: lichx@hit.edu.cn (C. Li).

candidates for the production of proportionally tunable syngas. And exploring suitable elemental compositions is highly significant for designing bimetallic chalcogenides for efficient ECO₂RR.

Unfortunately, slow kinetic processes and high overpotentials lead to low current density and weak binding between the reaction intermediates and catalyst active sites. These factors are related to the intrinsic electronic structure and properties of the catalyst as well as the properties of the employed electrolyte [16]. Many studies have confirmed that Keggin-type polyoxometalates (POMs) can serve as important electron modulators [19]. POMs can interact with CO₂(l) [20] to improve its solubility and enhance the catalytic activity for ECO₂RR. For example, Sun et al. chose PV₃Mo₉ as an electrolyte additive coupled with a commercial indium electrode to realize ECO₂RR. The electron transfer process of the substituted V atom in PV₃Mo₉ effectively promoted the activation of CO₂ molecules and the Faradaic efficiency (FE) of ethanol [21]. However, the other side of the interaction between PV₃Mo₉ and the commercial indium electrode also caused a severe hydrogen evolution reaction (HER) and instability at higher potentials. Based on the above reports, it is found that PV₃Mo₉ can solve the problem of bimetallic chalcogenides' application in dynamics. And bimetallic chalcogenides have much higher stability than indium, and it is expected to alleviate the serious HER caused by the oxidation of PV₃Mo₉ on electrodes at higher overpotential. In addition, Debergh et al. has found that, among low-temperature ECO₂RR technologies that produce syngas, the route integrating capture with conversion is more economical than the sequential routes [22]. Taking a project of comprehensive utilization of 55000 Nm³/h coke oven gas in a 2 million ton/year coking plant as an example, this work which combines CO₂ capture by POM [23] and catalytic conversion by bimetallic chalcogenides, can reduce CO₂ emissions by 5820 Nm³/h and save \$3.47 million per year in operation cost.

Herein, three bimetallic chalcogenides with different elemental compositions (MInX₂: CuInSe₂, AgInS₂, and CuInS₂) were prepared through a simple one-step synthesis method and combined with a PV₃Mo₉ medium to achieve proportionally tunable syngas. PV₃Mo₉ has been proven to contribute to kinetics. Unlike AgInS₂ and CuInS₂, CuInSe₂ showed metal-like characteristics with overlapping valence and conduction bands. Due to the interaction between In and Cu orbitals, the adsorption of intermediates on the surface of CuInSe₂ was moderated, thereby further optimizing the ECO₂RR performance. In summary, bimetallic chalcogenides show promising prospects as active and low-cost materials for ECO₂RR in this cutting-edge field. And this work shows that the promising prospects of efficient combinations of electrolyte and electrode materials as the next frontier for improving ECO₂RR activity and economic efficiency.

2. Experimental

2.1. Materials

All chemicals were used without any purification. Sodium molybdate (Na₂MoO₄·2 H₂O), sodium metavanadate (NaVO₃), disodium hydrogen phosphate (Na₂HPO₄·12 H₂O), sodium sulfate (Na₂SO₄), silver nitrate (AgNO₃), indium nitrate (In(NO₃)₃), cuprous chloride (CuCl), indium chloride (InCl₃) and selenium powder (Se) were purchased from Shanghai Aladdin Bio-Chem Technology Co., Ltd. Sublimated sulfur (S), oleylamine (OA), thioacetamide (TAA), ethylenediamine (EDA), diethyl ether, N,N-dimethylformamide (DMF), and concentrated sulfuric acid (H₂SO₄) were obtained from Sinopharm Chemical Reagent Co., Ltd. Dimethyl sulfoxide (DMSO) and deuterium oxide (D₂O) were purchased from Shanghai Macklin Biochemical Technology Co., Ltd. DMSO and D₂O were high-purity liquid chromatography (HPLC) grade, while the other chemicals were analytically pure. Carbon cloth (W0S1011), carbon black (Vulcan XC-72), gas diffusion layer (Freudenberg, H23C9) and proton exchange membrane (Nafion 117) were purchased from Shanghai Hesen Electric. High-purity argon gas (Ar, 99.999%) and CO₂

(99.999%) were purchased from Harbin Liming Gas Co., Ltd. Deionized water was used during the whole experiment.

2.2. Synthesis of PV₃Mo₉

PV₃Mo₉ was synthesized based on the method reported in the literature [21]. An 80 mL mixed solution containing Na₂HPO₄·12 H₂O (0.01 M) and Na₂MoO₄·2 H₂O (0.09 M) was refluxed for 0.5 h. Excess NaVO₃ (0.035 M, 20 mL) was added to the mixed solution, which was refluxed for an additional 0.5 h. 50% (volume fraction) dilute H₂SO₄ was used to adjust the pH of the solution to 2.5 ± 0.1. This mixed solution was extracted with ether to collect the red oil droplets at the bottom layer. The 50% dilute H₂SO₄ solution was repeatedly added to the extraction system until the aqueous phase turned light yellow. The ether in the collected droplets was removed in air, and the product was then dried and purified by concentrated crystallization to yield PV₃Mo₉.

2.3. Synthesis of AgInS₂, CuInSe₂ and CuInS₂

CuInSe₂ was prepared according to the method reported in the literature [24]. 12 mL OA was added into a three-necked flask and degassed at 130 °C for 30 min, followed by purging with Ar several times. CuCl solution (0.4 M, 5 mL OA) and InCl₃ solution (0.4 M, 5 mL OA) were added to the flask, followed by purging with Ar several times. This solution was continually stirred and heated to 285 °C. Then, 2 mL of 2 M Se powder suspended in OA was injected into the flask. The system was maintained at 285 °C for 30 min under 30 mL/min Ar flow. Next, the mixture was cooled to 60 °C, and n-hexane and ethanol were added to flocculate the crystals. The obtained suspension was centrifuged at 8000 r for 10 min and dried at 60 °C for 12 h to obtain CuInSe₂ crystals. The synthesis route scheme is shown in Fig. S1.

AgInS₂ was prepared via the modified method reported in the literature [18]. Briefly, 20 mL OA was added into a three-necked flask and degassed at 130 °C for 30 min under Ar. The cation solution (0.5 M AgNO₃ and 0.5 M In(NO₃)₃ dissolved in 10 mL OA) and the anion solution (0.5 M S power dissolved in 0.5 mL ethylenediamine and 10 mL OA) were injected into the flask under continuous stirring. This solution system was purged with Ar for 20 min and heated to 230 °C for 30 min within 1 h under Ar atmosphere. The solution was continuously stirred and cooled to 60 °C, and n-hexane and ethanol were alternately drop-wise added into the flask during the cooling process. The obtained suspension was centrifuged at 8000 r for 10 min and dried at 60 °C for 12 h to obtain AgInS₂ crystals. The synthesis route scheme is presented in Fig. S2.

CuInS₂ was synthesized via the solvothermal method [25]. Briefly, 2 mM InCl₃, 2 mM CuCl, and 4 mM TAA were dissolved in 40 mL DMF. This mixed solution was vigorously stirred at room temperature for 60 min and then transferred to an autoclave. The autoclave was sealed and heated at 160 °C for 12 h. Then, the autoclave was cooled to room temperature, and the precipitate was washed with deionized water and ethanol several times. The washed precipitate was then dried at 60 °C for 12 h. The synthesis route scheme is exhibited in Fig. S3.

2.4. Preparation of working electrode

A mixture of 500 μL isopropanol and 30 μL Nafion solution (5%) was ultrasonicated for 30 min. 4 mg catalyst and 2 mg carbon black were added to the isopropanol and Nafion mixture, which was then ultrasonicated again for 30 min to form an evenly dispersed ink. 200 μL of the ink was coated on a tailored carbon cloth (1.5 cm × 1 cm × 2) by a pipette gun and dried at 60 °C for 12 h. The loading capacity of the catalyst was determined by the weight difference before and after coating.

2.5. Characterization methods

The morphologies of the prepared catalysts were analyzed by field emission scanning electron microscopy (SEM, ZEISS, SUPRA 55) equipped with energy-dispersive X-ray spectroscopy (EDS) mapping and high-resolution transmission electron microscopy with a spherical aberration corrector (HRTEM, Japan-JEOL-JEM 2100 F). The element compositions of the catalysts were characterized by inductively coupled plasma mass spectrometry (ICPMS, PerkinElmer, NexION 350X). Powder X-ray diffraction (XRD) patterns were collected by X-ray diffractometry (Bruker, D8 Advance) with Cu K α radiation ($\lambda = 1.5406 \text{ \AA}$) at a scan rate of 10° (20) per minute. Further electron properties were explored by X-ray photoelectron spectroscopy (XPS, ThermoFisher, Escalab 250 XI), and all binding energies were calibrated by the C 1 s signal of organic contamination on the sample surface (284.6 eV).

2.6. In situ characterization technology

In situ surface-enhanced Raman spectra (SERS) were recorded with a Raman spectrometer (HORIBA, LabRAM Soleil) equipped with a 532 nm wavelength laser. The potential-related Raman spectra were collected every 5 min with a potential gradient of 0.05 V. The *in-situ* Raman electrolysis cell consisted of three electrodes, including a working electrode (CuInSe₂), counter electrode (Pt wire), and reference electrode (Ag/AgCl). The working electrode was prepared by loading 1 mg/cm² catalyst on a glassy carbon electrode. The electrolyte was CO₂-saturated 0.1 M Na₂SO₄ solution containing 2 mM PV₃Mo₉.

The electrochemical *in-situ* Fourier transform infrared (FTIR) spectra were monitored by Shimadzu (IR Tracer100) equipped with an *in-situ* electrolytic cell. The treated carbon cloth, Ag/AgCl electrode, and Pt sheet were used as the working, reference, and counter electrodes, respectively. The electrolyte was 0.1 M Na₂SO₄ containing 2 mM PV₃Mo₉, and the applied potential was controlled by the electrochemical workstation (Chenhua, CHI 660E). During the electrochemical *in-situ* FTIR experiments, Ar was blown into the electrolyte for at least 30 minutes to remove any impure gas. Next, the potential was applied to the working electrode, and the FTIR spectra were continuously collected until a time-independent signal was obtained. At this point, the background spectrum was collected under continuous purging of CO₂ into the cell. Subsequently, *in-situ* FTIR spectra were collected as a function of time.

2.7. Electrochemical tests and product analysis

The selection of electrocatalysts is usually carried out in a conventional H-type cell [26]. In order to observe the experimental phenomena more directly and evaluate the ECO₂RR activity of electrocatalysts in different solution mediums, a series of electrochemical tests of the prepared catalysts were carried out in a quartz H-type electrolytic cell which is more convenient to assemble. The H-type cell is composed of cathode and anode chambers separated by a Nafion 117 membrane. The anolyte was 0.1 M dilute H₂SO₄ (30 mL), and the catholyte was 0.1 M Na₂SO₄ (30 mL) with or without 2 mM PV₃Mo₉. Before each test, the cell was purged with Ar for 30 min with a flow rate of 20 sccm to remove impurities. Then, CO₂ (99.999%) was bubbled into the cathode for 30 min with a flow rate of 20 sccm to reach saturation. All electrochemical measurements were conducted on an electrochemical analyzer (Donghua Test, DH-7000) with a three-electrode test system. The treated carbon cloth, a platinum sheet, and an Ag/AgCl electrode were employed as the working, counter, and reference electrodes, respectively. The reversible hydrogen electrode (RHE) potential was converted as follows:

$$V_{(\text{RHE})} = V_{(\text{Ag/AgCl})} + 0.0591 \times \text{pH} + 0.197 \text{ V.} \quad (1)$$

The flow cell can overcome the mass transfer limitations of the H

type cell by continuously circulating reactants and products to and from the electrode, thereby achieving higher CO₂ concentrations on the electrocatalyst surface to optimizes the dynamics process [26]. Therefore, ECO₂RR tests were carried out in a flow electrolytic cell, as exhibited in Fig. S4. The flow cell was composed of a gas flow chamber, a cathode liquid flow chamber, an anode chamber, a piece of Nafion 117 membrane, gaskets, and a back panel. The chambers and the back panel were composed of polytetrafluoroethylene (PTFE). The catholyte and anolyte chambers were 1 cm thick and contained a 4 cm × 4 cm window. The flow cell was filled with 15 mL catholyte and 15 mL anolyte. A peristaltic pump was installed outside the cathode chamber to drive the cathode liquid flow with a flow rate of 2 mL·min⁻¹. CO₂ was bubbled into the system with a flow rate of 20 sccm. A gas diffusion electrode (GDE) was used for the working electrode with a similar preparation method in Section 2.4, except that the ink was loaded on the gas diffusion layer instead of carbon cloth. The geometric area of the working electrode in contact with the catholyte was 1 cm². A platinum sheet and Ag/AgCl electrode were used as the counter and reference electrodes, respectively.

The gas products were analyzed by an on-line gas chromatograph (BF SP-2100A, equipped with a conversion furnace, TCD and FID detector). High-purity Ar was used as the carrier gas. The Faradaic efficiencies (FEs) of the gas products were calculated according to the following equation:

$$FE = x_i \times V \times t \times \frac{2Fp}{QRT} \times 100\% \quad (2)$$

where x_i represents the concentration of CO or H₂ obtained by gas chromatography, V is the flow rate of CO₂, t is the electrolysis time, Q denotes the amount of charge consumed during electrolysis, F = 96485 C·mol⁻¹, p = 101325 Pa, R = 8.314 J/(mol·K), and T = 298.15 K.

The liquid products were collected and analyzed by ¹H nuclear magnetic resonance (¹H NMR, BRUKER, AV-400) using D₂O as the deuterated solvent and DMSO as the internal standard species. The concentrations of the liquid products were measured by a previous standard curve obtained on the same instrument [21]. The FEs were calculated as follows:

$$FE(\%) = \frac{z_i n_i F}{Q} \times 100\% \quad (3)$$

where n_i is the amount of product (mol) obtained by ¹H NMR and z_i is the number of transferred electrons required to obtain 1 mol product. The error estimates of the FEs were obtained from three repeated measurements under the same experimental conditions.

Turnover frequency (TOF), energy efficiency (EE) and carbon conversion efficiency (CCE) are important indicators for evaluating catalyst performance, and they were calculated as follows:

$$TOF(h^{-1}) = \frac{I_{\text{product}}/nF}{m_{\text{cat}} \times \omega/M_{\text{metal}}} \times 3600 \quad (4)$$

where I_{product} is the partial current for CO (A), n is the number of electrons transferred for CO (2), F is the Faradaic constant (96485 C/mol), m_{cat} is the catalyst mass in the electrode, ω is the mass percentage of active metal atoms in the catalyst, and M_{metal} is the atomic mass of the metal [27–29].

$$EE(\%) = \frac{1.23 - E_0}{1.23 - E} \times FE(\%) \times 100\% \quad (5)$$

where E_0 is the standard potential (CO, −0.11 V), E is the applied potential, and FE is the Faradaic efficiency [28].

$$CCE(\%) = \frac{\sum n_{c,\text{products}}}{\Delta n_{c,\text{substrate}}} \times 100\% \quad (6)$$

where $\sum n_{c,\text{products}}$ is the sum of the molar amount of all the carbon

products obtained by GC and ^1H NMR, $\Delta n_{c,\text{substrate}}$ is the amount of carbon within the gaseous CO_2 fed during 60 min of experiment. It is calculated as follows:

$$\Delta n_{c,\text{substrate}} = \frac{pV}{RT} \quad (7)$$

where V represents the volume of the gas depending on the flow rate during 60 min in m^3 ; $p = 101325 \text{ Pa}$, $R = 8.314 \text{ J}/(\text{mol}\cdot\text{K})$, and $T = 298.15 \text{ K}$ [30].

2.8. DFT calculations

All spin-polarized density functional theory (DFT) calculations were performed by the Vienna Ab initio Simulation Package (VASP) [31] with the projector augmented wave (PAW) method [32]. The exchange-functional was treated using the generalized gradient approximation (GGA) with the Perdew-Burke-Ernzerhof (PBE) [33] functional. The energy cutoff for the plane wave basis expansion was set to 500 eV. Partial occupancies of the Kohn-Sham orbitals were allowed using the Gaussian smearing method and a width of 0.05 eV. The vacuum spacing of the surfaces in the direction perpendicular to the plane of the structure was 15 Å. Brillouin zone integration was performed using $2\times 2\times 1$ Monkhorst-Pack k-point sampling for each structure. A convergence energy threshold of 10^{-4} eV was applied for the self-consistent calculations, and the force convergency was set to 0.05 eV/Å.

The reaction free energy was calculated following the computational hydrogen electrode (CHE) model [34]. The free energy corrections were considered at a temperature of 298 K, as follows:

$$\Delta G = \Delta E + \Delta GZPE + \Delta GU - T\Delta S \quad (8)$$

where ΔE is the DFT calculated energy change, $\Delta GZPE$ is the correction from zero-point energy, ΔGU is the correction from inner energy, and ΔS

is the correction from entropy.

3. Results and discussion

3.1. Characterizations of the prepared $M\text{In}X_2$

CuInSe_2 was synthesized through an improved thermal injection process using OA as the solvent and reducing agent. As presented in Fig. 1(a), the diffraction peaks of the synthesized CuInSe_2 are consistent with those of chalcopyrite CuInSe_2 (PDF-# 40-1487). The diffraction peaks at 26.61° , 44.16° , 44.25° , 52.26° and 52.41° correspond to the characteristic (112) , (204) , (220) , (116) , and (312) planes of the chalcopyrite structure, respectively, in good agreement with previously reported work [24]. This XRD pattern demonstrates that CuInSe_2 crystallizes in the tetragonal phase (space group: $I\bar{4}2d$), and the crystal structure is shown in the Fig. 1(a) inset. SEM analysis (Fig. S5) reveals that CuInSe_2 forms agglomerated spherical particles. All precursors were added at low temperatures, and the temperature was gradually increased to the final growth temperature. Thus, crystal nucleation and growth were not expected to be uniform [24]. In addition, the lattice fringes with an interplanar distance of $\sim 0.335 \text{ nm}$ was observed in the TEM image (Fig. 1(b)), and the fringe spacing corresponds to the (112) plane of the tetragonal CuInSe_2 crystal phase, suggesting that the growth direction of CuInSe_2 crystal is along $[112]$ [16]. The elemental mapping result (Fig. 1(c)) manifest uniform distribution of Cu, In and Se in the CuInSe_2 crystal. The electronic characteristics and composition of CuInSe_2 were explored by XPS. As displayed in Fig. S6, the characteristic peaks at binding energies of 932.4 and 952.3 eV correspond to $\text{Cu } 2p_{3/2}$ and $\text{Cu } 2p_{1/2}$, respectively [35]. $\text{Cu } 2p_{3/2}$ with a binding energy of 932.4 eV can be classified as Cu^0 or Cu^+ . Due to the close binding energies of Cu^0 and Cu^+ on the 2p orbital, it is difficult to determine the valence state of Cu through the Cu 2p spectrum. The shift of the Auger peak between Cu^0 and Cu^+ exceeds 1 eV, which is often used to determine the valence state of Cu [36]. The peak located at 569.7 eV in Fig. 1

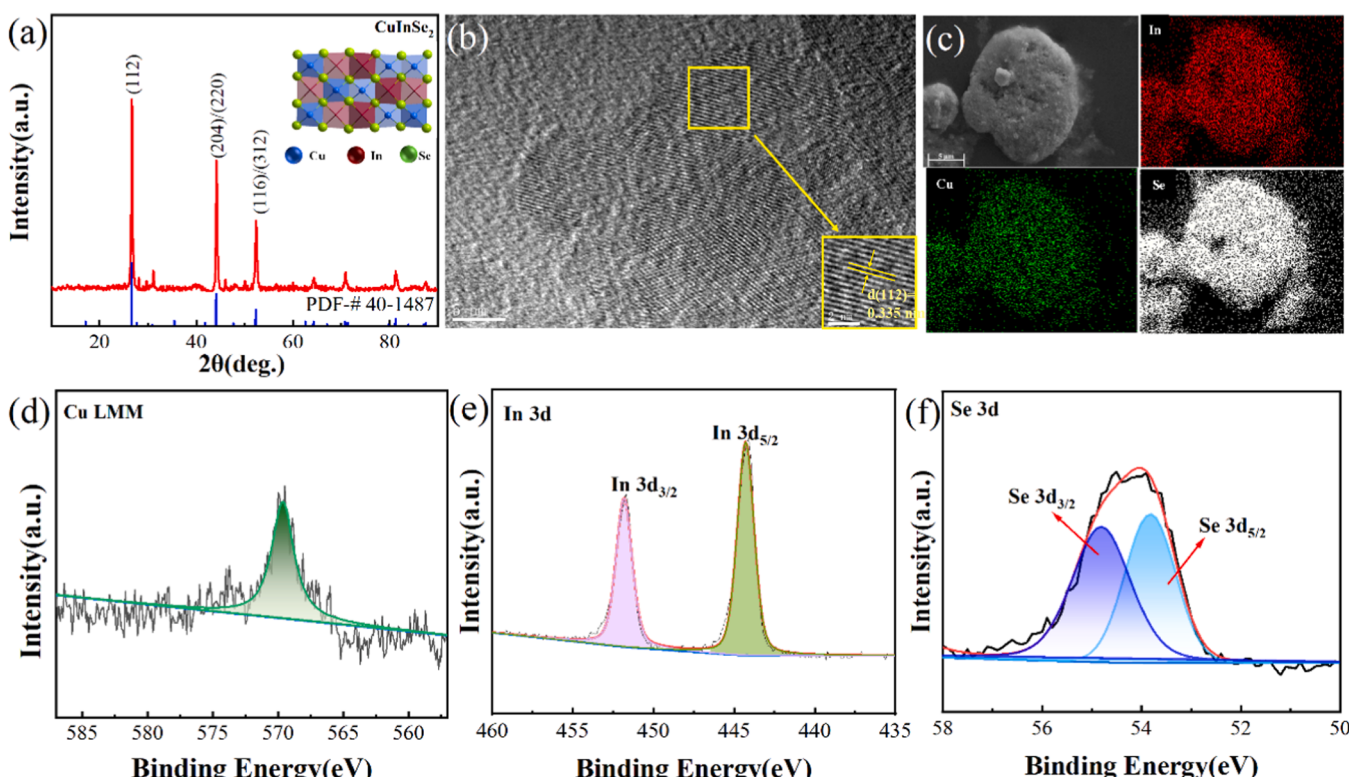


Fig. 1. Characterization of synthesized CuInSe_2 crystal. (a) XRD pattern, inset: crystal structure; (b) TEM image; (c) elemental mapping; (d) Cu LMM, (e) In 3d and (f) Se 3d high resolution XPS spectra.

(d) belongs to Cu⁺, proving that the valence state of Cu in CuInSe₂ is +1 [37]. The binding energy positions of In 3d_{3/2}, In 3d_{5/2}, Se 3d_{3/2}, and Se 3d_{5/2} are located at 451.8, 444.1, 54.8 and 53.9 eV, respectively (Fig. 1 (e, f)) [18,38]. These results illustrate that the chemical valence states of the In and Se in CuInSe₂ are In³⁺ and Se²⁻ [38]. The elemental composition results obtained through SEM, XPS, and ICPMS (Table S1) confirm that the stoichiometric ratio of Cu: In: Se in CuInSe₂ is 1:1:2. In summary, these results verify the structure and composition of the synthesized CuInSe₂ crystal, indicating the successful preparation of chalcopyrite CuInSe₂.

AgInS₂ and CuInS₂ crystals were prepared by improved thermal injection and solvothermal methods, respectively. The XRD patterns in Fig. S7(a) and Fig. S9(a) demonstrate that the synthesized AgInS₂ crystallizes in the orthorhombic crystal system (space group: *Pna2*₁) [39], while CuInS₂ crystallizes in the tetragonal phase (space group: *I-42d*) [40]. The crystal structures of AgInS₂ and CuInS₂ are shown in the insets of Fig. S7(a) and Fig. S9(a). SEM results elucidate that AgInS₂ forms a stacked sheet structure (Fig. S8), while CuInS₂ exhibits spherical particles (Fig. S10). Moreover, lattice fringes of 0.335 nm are observed in the TEM image of AgInS₂ (Fig. S7(b)), with fringe spacing

corresponding to the (002) plane of the orthogonal AgInS₂ crystal phase, indicating that the growth direction of the AgInS₂ crystal is along the [002] direction [16]. The lattice fringes of 0.312 nm observed in Fig. S9 (b) corresponding to the (112) crystal plane, indicating that the growth of the CuInS₂ crystal is along the [112] direction [16]. The elemental mapping results of both crystals depict the uniform distribution of each element (Fig. S7(c) and S9(c)). XPS was performed to further evaluate the electronic structures and elemental valence states of AgInS₂ and CuInS₂. As indicated in Fig. S7(c-f) and S9(c-f), the valence states of Ag, In, and S in AgInS₂ are +1, +3, and -2, respectively [41], while the valence states of In, and S in CuInS₂ are +3, and -2, respectively. The valence state of Cu in CuInS₂ is +1, which is verified by the peak located in 569.8 eV in Cu LMM spectrum in Fig. S11 [37]. The atomic percentages of each element in AgInS₂ and CuInS₂ are summarized in Tables S2 and S3. The proportions of each element in these two crystals match the theoretical values. In summary, these results verify the structure and composition of the synthesized AgInS₂ and CuInS₂, implying that they were successfully prepared.

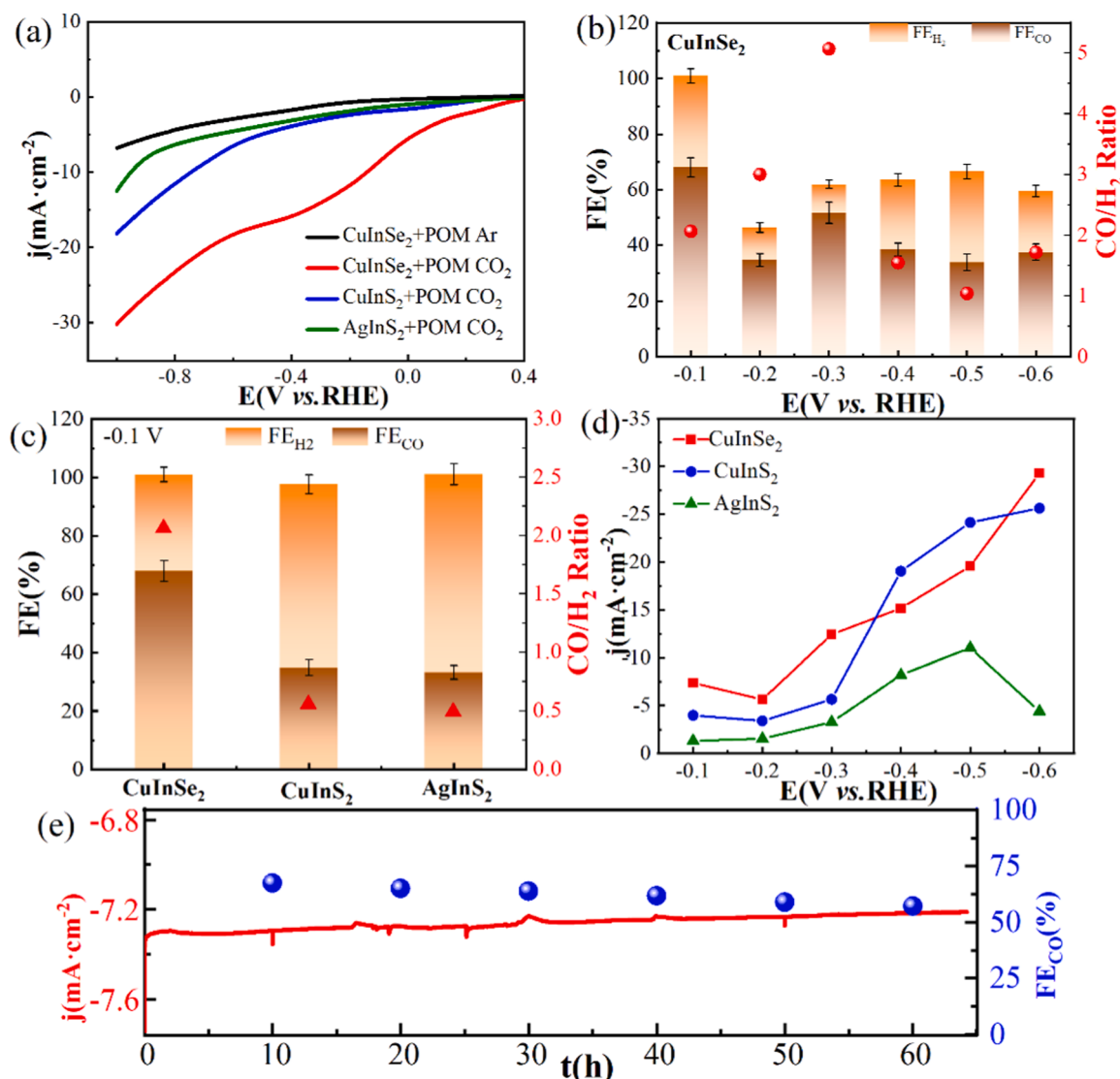


Fig. 2. (a) LSV curves of CuInSe₂ in POM medium under Ar/CO₂ atmosphere with a scan rate of 100 mV·s⁻¹; (b) FEs (CO and H₂) and CO/H₂ ratio of CuInSe₂ in POM medium after electrolysis for 1 h at -0.1–0.6 V (vs. RHE) in a flow cell; (c) FEs (CO and H₂) and CO/H₂ ratio of MInX₂ in POM medium after electrolysis for 1 h at -0.1 V (vs. RHE); (d) j_{CO} of MInX₂ in POM medium after electrolysis for 1 h at -0.1–0.6 V (vs. RHE) in a flow cell; (e) stability test of CuInSe₂ in POM medium electrolysis at -0.1 V (vs. RHE) in a flow cell.

3.2. Electrocatalytic properties of $MInX_2$ in aqueous and POM media for ECO_2RR

Linear sweep voltammetry (LSV) curves of $MInX_2$ were obtained in both aqueous (0.1 M Na_2SO_4) and POM media using carbon cloth electrodes (note: the POM media is 0.1 M Na_2SO_4 solution containing 2 mM PV_3Mo_9 , which contributes to the maximum ECO_2RR activity [21]). As displayed in Figs. S12, S13, and 2(a), the LSV curves of $MInX_2$ in CO_2 atmosphere exhibit higher current densities than those in Ar, implying the high activity of $MInX_2$ towards ECO_2RR in both media. The onset potentials of $MInX_2$ -catalyzed ECO_2RR in POM medium are significantly lower than those in the aqueous medium, suggesting that PV_3Mo_9 effectively assists the cathodic dynamics, which reduces energy consumption and the energy barriers for electron transfer [42]. Additionally, $CuInSe_2$ in POM medium exhibits the highest current density (-30.2 mA·cm⁻², normalized by geometric surface area) under CO_2 atmosphere, as shown in Fig. 2(a). The current density of $CuInSe_2$ in POM under CO_2 is roughly 1.7 and 2.5 times higher than that of $CuInS_2$ (-18.1 mA·cm⁻²) and $AgInS_2$ (-12.3 mA·cm⁻²), respectively. This confirms that $CuInSe_2$ has the highest ECO_2RR activity in the POM medium [16].

However, these LSV results are not sufficient for verifying the high catalytic activity of $CuInSe_2$ towards ECO_2RR , as HER and ECO_2RR are usually interconnected simultaneously. Therefore, the actual activity of $MInX_2$ in the POM medium toward ECO_2RR was investigated by loading each catalyst onto a GDE in a flow cell at an applied potential of -0.1–0.6 V (vs. RHE). GC results indicate that syngas (CO and H_2) evolves in all three systems. Moreover, as indicated by ¹H NMR analysis, a small amount of ethanol is also generated in the $CuInS_2$ and $CuInSe_2$ systems (Fig. S14). According to comparative experiments, the carbon source of the products is the CO_2 introduced into the system (Fig. S15). Fig. 2(b) and Fig. S16(a, b) show the FEs of syngas and the obtained CO/ H_2 ratios as functions of applied potential. $CuInSe_2$ in the POM medium has the highest FE_{CO} (~68.0%) at an ultra-low potential of -0.1 V (vs. RHE). This FE_{CO} value is 1.7 and 1.2 times higher than those of $CuInS_2$ (~41.2%) and $AgInS_2$ (~57.8%) in the POM medium, respectively. Moreover, the $CuInSe_2$ system has the widest CO/ H_2 ratio range (1.0–5.1) compared to the $CuInS_2$ (0.3–1.2) and $AgInS_2$ (0.2–1.5) systems. As shown in Fig. 2(b), the FE_{CO} value decreases at -0.2 V (vs. RHE). This is due to the generation of ethanol, which has an FE value of 51.6% (Fig. S16(c)). The FE_{CO} and CO/ H_2 ratios of $MInX_2$ in the POM medium at an ultra-low applied potential of -0.1 V (vs. RHE) are summarized in Fig. 2(c), clearly demonstrating the energy consumption advantage of $CuInSe_2$ for achieving the highest FE_{CO} . Fig. 2(d) shows the CO partial current density (j_{CO}) of $MInX_2$ in the POM medium in the range of -0.1–0.6 V (vs. RHE). All three systems clearly show selective catalytic activity for CO formation during ECO_2RR . The maximum j_{CO} of $CuInSe_2$ in the POM medium is -29.3 mA·cm⁻², which is ~1.2 times and 2.7 times higher than that of $CuInS_2$ (-25.6 mA·cm⁻²) and $AgInS_2$ (-11.0 mA·cm⁻²) in the POM medium. This result undoubtedly proves the high activity of $CuInSe_2$ in POM medium toward ECO_2RR .

To evaluate the stability of $CuInSe_2$ toward ECO_2RR , chronocurrent measurements were carried out over an extended period of more than 60 h at -0.1 V (vs. RHE) in the POM medium in a flow cell (Fig. 2(e)). After the stability test, the FE_{CO} decays to 57.2% (a loss of 10.3% compared to the initial state). This attenuation may be caused by partial blockage of the catalyst's active sites after prolonged testing. XPS analysis of the electrode after the stability test (Fig. S17) does not show any valence state changes in $CuInSe_2$, suggesting that the electronic structure of $CuInSe_2$ in the POM medium is stable during ECO_2RR . This demonstrates that the POM medium improves the kinetics of ECO_2RR and interacts with CO_2 molecules rather than with the electrode [20]. In addition, $CuInSe_2$ does not display any morphological (Fig. S18) or structural (Fig. S19) changes in the POM medium, indicating its good stability in the POM medium for ECO_2RR . The performance comparison between this work and the recently reported researches on the synthesis

of syngas using transition metal chalcogenides in ECO_2RR is summarized in Table S4. It is observed that this work is progressiveness in terms of energy saving and syngas ratio.

3.3. Kinetics analysis of $MInX_2$ in POM and aqueous media for ECO_2RR

To gain better insight into the dynamics of CO formation, the Tafel slopes of $MInX_2$ in both the aqueous and POM media were obtained, as shown in Fig. 3(a, b). The Tafel slopes of $MInX_2$ in the POM medium are significantly lower, indicating that the addition of PV_3Mo_9 further accelerates charge transfer and improves the electrocatalytic activity. As reported, the activation of $CO_2(l)$ molecules is accelerated by the coordination effect between POM and $CO_2(l)$ [20], which reduces the energy input required for ECO_2RR in the POM medium. Consequently, the onset potential significantly decreases, which is confirmed by the LSV results in Section 3.2.

The formation of the *COOH intermediate (a single-electron transfer process) has been identified as the rate-determining step (RDS) for CO evolution due to its higher reaction energy barrier compared with other steps [28]. The Tafel slope of $CuInSe_2$ in the aqueous medium is 265 mV·dec⁻¹, while the Tafel slopes of $CuInS_2$ and $AgInS_2$ in the POM medium are 239 mV·dec⁻¹ and 244 mV·dec⁻¹, respectively. In comparison, $CuInSe_2$ in the POM medium shows a much lower Tafel slope of 115 mV·dec⁻¹, which is slightly lower than the theoretical value of 118 mV·dec⁻¹ expected for the RDS at the electrode [43]. This suggests faster kinetics for the formation of the *COOH intermediate. To further investigate other factors for the excellent catalytic performance of $CuInSe_2$, the electrochemical double-layer capacitance (C_{dl}) was measured to analyze the electrochemical active surface area (ECSA) of each catalyst (Fig. S20). The C_{dl} value of $CuInSe_2$ (0.73 mF·cm⁻²) is higher than that of $CuInS_2$ (0.59 mF·cm⁻²) and $AgInS_2$ (0.31 mF·cm⁻²), confirming that $CuInSe_2$ has the largest ECSA. Thus, $CuInSe_2$ contains more active sites for the adsorption of intermediates to accelerate the kinetic process [19]. Moreover, electrochemical impedance spectroscopy (EIS) was used to evaluate $MInX_2$ in the POM medium under a CO_2 atmosphere to further evaluate the electrode reaction kinetics. As presented in Fig. 3(c), the Nyquist curve of $CuInSe_2$ in POM has the smallest semicircle diameter, manifesting the fastest charge transfer rate [21]. Accordingly, the Faraday process of $CuInSe_2$ in the POM medium is faster than that of the other two systems during the ECO_2RR process. Furthermore, as important evaluation parameters for the performance of catalysts in renewable energy storage, the turnover frequency (TOF) and energy efficiency (EE) of $MInX_2$ in the POM medium were calculated, as shown in Fig. S21. The maximum TOF and EE values of $MInX_2$ are summarized in Fig. 3(d). The TOF_{max} of $CuInSe_2$ in the POM medium is -517.0 h⁻¹, which is ~1.6 and 4.3 times higher than that of $CuInS_2$ (-326.1 h⁻¹) and $AgInS_2$ (-120.4 h⁻¹), respectively. In addition, the EE_{max} of $CuInSe_2$ in the POM medium is 68.5%, which is higher than that of $CuInS_2$ (~35.2%) and $AgInS_2$ (~50.6%) in the POM medium. Carbon Conversion Frequency (CCE) is also an important indicator for the performance of ECO_2RR catalysts. The CCE values of $MInX_2$ in POM medium at -0.1–0.6 V (vs. RHE) are summarized in Fig. S22. The CCE_{max} of $CuInSe_2$ in POM medium is 2.6%, which is ~1.1 and 3.3 times higher than that of $CuInS_2$ (2.3%) and $AgInS_2$ (0.8%), respectively. Overall, these results confirm that $CuInSe_2$ in the POM medium stands out among the state-of-the-art catalysts for the evolution of syngas via ECO_2RR to evolve syngas.

3.4. Origins of enhanced ECO_2RR performance

To visually comprehend the enhancement of ECO_2RR by $CuInSe_2$, the intermediates and other substances ($CuInSe_2$ and POM) during ECO_2RR were monitored in real-time by *in situ* SERS in CO_2 -saturated POM medium from 0–0.5 V (vs. RHE). In the Raman spectrum obtained under the open current potential (Fig. S23), two bands centered at 178 and 230 cm⁻¹ correspond to the A_1 and E lattice vibrational modes of

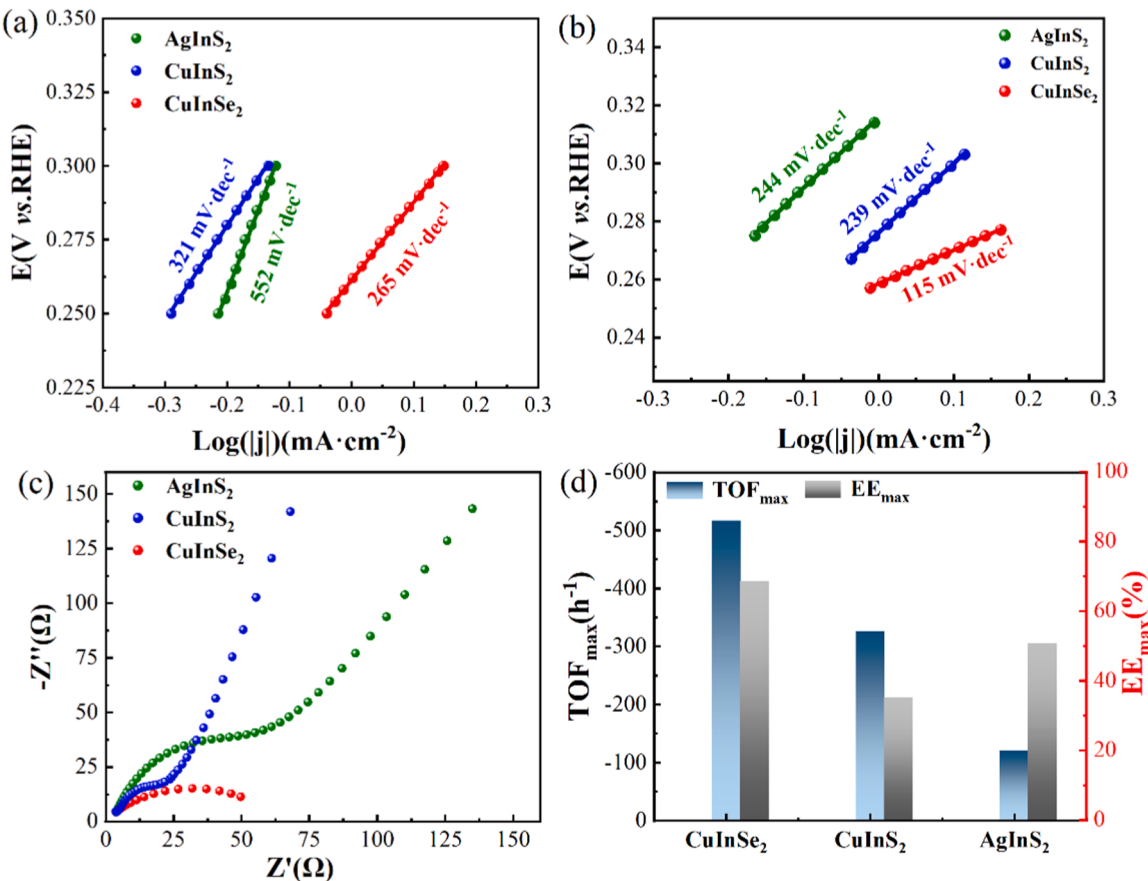


Fig. 3. Tafel slopes of MInX₂ in CO₂-saturated (a) 0.1 M Na₂SO₄ and (b) POM medium; (c) Nyquist curves of MInX₂ in CO₂-saturated POM medium; (d) the values of TOF_{max} and EE_{max} of MInX₂ in POM medium.

CuInSe₂, respectively [44]. Two additional bands at 253 cm⁻¹ (Fig. S23 inset) and 979 cm⁻¹ are ascribed to the v_s (Mo-O_a) and v_{as} (Mo-O_b) vibrations of PV₃Mo₉ [45]. The intensities and position of these four bands are maintained during the in situ SERS detection period, as presented in Fig. 4(a, b). This further confirms the structural stability of CuInSe₂ and PV₃Mo₉.

As observed in Fig. 4(a), the initial potential only shows the Raman peaks of CuInSe₂ and PV₃Mo₉. When the applied potential is negatively shifted to -0.1 V (vs. RHE), new peaks appear at 359 cm⁻¹ (v Cu-C), 1559 cm⁻¹ (v_{as} CO₂) and 1050 cm⁻¹ (v CO₃²⁻) [46]. The v CO₃²⁻ peak is caused by the dissociation equilibrium of CO₂ in the system [46]. Interestingly, the v Cu-C peak and v_{as} CO₂ peak show similar intensity trends with time, indicating that these peaks are associated with the same species. As reported, the signal at 359 cm⁻¹ is assigned to the vibration of Cu-C bonding in the *CO₂ intermediate, where the C atom is coordinated with the Cu [47]. As the reaction time increased and the potential shifted negatively, a symmetric stretching *COOH vibrational peak appears at 1370 cm⁻¹. The gradually weaker intensity of this peak is attributed to the conversion of *COOH to *CO. Additionally, a broad band centered at 720 cm⁻¹ with a shorted occurrence time caused by the weak adsorption was belonged to the in-plane bending vibration mode of CO₂ (δ CO₂) [46]. Meanwhile, the peak of v Cu-OH at 522 cm⁻¹ was detected in the range of -0.4–0.5 V (vs. RHE), resulting from the increase in local pH [48]. The presence of v Cu-OH is beneficial for increasing the charge balance between C atoms in the O*CCO intermediate, further promoting C-C coupling and the selectivity of C2 products [48]. These in situ SERS results demonstrate the intermediates and reaction pathway of CO evolution (Fig. 4(c)). However, the high ECO₂RR activity of CuInSe₂ in POM medium still requires further exploration to verify.

In order to further understand the mechanism of action of POM and the competition between ECO₂RR and HER, in-situ FTIR was conducted during 2 h ECO₂RR process driven by CuInSe₂ in POM medium at -0.5 V (vs. RHE). At this potential, both ECO₂RR and HER would be clearer, and C2 products were generated to make the related intermediates more prominent in the spectra. As shown in Fig. 5(a), the two bands that always appear at 2343 cm⁻¹ and 1650 cm⁻¹ are attributed to the vibrations of dissolved CO₂ and water molecules, respectively [21]. As the reaction proceeds, three other bands are recorded at 1961, 1735, and 1606 cm⁻¹, belonging to C=O bond of linear *CO_L, C=O bond of bridge *CO_B, and the bending vibration of *OH adsorbed on the catalyst surface, respectively [37]. In addition, at the end of the reaction, two other bands located at 1421 and 1338 cm⁻¹ are observed, belonging to the stretching vibration of C=O bond of *CHO and C-H bond of *CH₃CH₂O, respectively [37]. These two bands provide a basis for the generation of ethanol. The absence of these five vibration bands in the early and late stages indicate the presence of adsorption intermediates in ECO₂RR.

It is worth noting that the peak positions of *CO_L and *CO_B gradually shift to higher wavenumber, while the peak position of *OH gradually shifts to lower wavenumber. This implies that the adsorption of *CO_L and *CO_B are enhanced while the adsorption of *OH is weakened, which can promote ECO₂RR and suppress HER, respectively [49]. But as the reaction time continues to increase, the peak positions of *CO_L and *CO_B gradually shift red, while the peak position of *OH shifts blue, representing the inhibition of ECO₂RR and the enhancement of HER. In order to clarify the reasons for these changes, four Keggin structural characteristic peaks of PV₃Mo₉ at 700–1100 cm⁻¹ were observed, representing the vibrations of P-O_a (1060 cm⁻¹), Mo-O_d (953 cm⁻¹), Mo-O_b-Mo (866 cm⁻¹), and Mo-O_c-Mo (786 cm⁻¹), respectively [21]. There is no

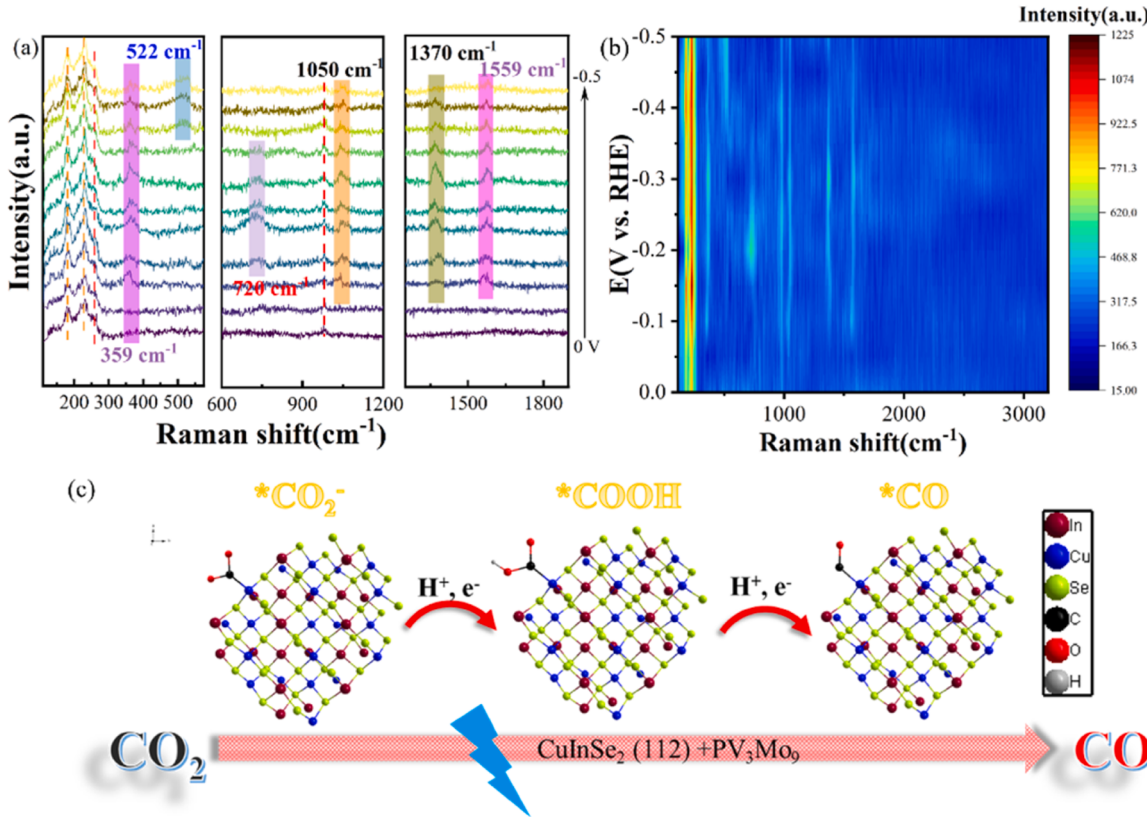
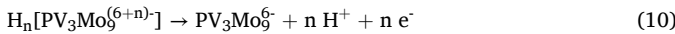


Fig. 4. (a) In-situ Raman spectra and (b) hot spot diagram of CuInSe₂ in POM medium in the range of 0–0.5 V (vs. RHE) with an interval of −0.05 V; (c) proposed mechanism scheme for ECO₂RR to CO on CuInSe₂ (112) in POM medium.

significant change in the peak intensity and position of P-O_a and Mo-O_d during the testing process. However, the peak intensities of Mo-O_b-Mo and Mo-O_c-Mo first increase and then decay, and the peak positions of Mo-O_c-Mo first shifts blue and gradually shifts red, indicating a reversible transition between POM and heteropoly blue [50]. In the early stage, PV₃Mo₉ obtained electrons and coupled protons to be reduced to heteropoly blue, with the following reaction formula:



This process weakens the *H adsorption at the interface and strongly inhibits HER, resulting in a relative increase in the adsorption of *CO_L and *CO_B, promoting ECO₂RR. Due to the reversible conversion between the POM and heteropoly blue [51], in the later stage, H_n[PV₃Mo₉⁽⁶⁺ⁿ⁾⁻] loses electrons and releases protons, with the following reaction formula:



This process leads to an increase in H⁺ at the interface, enhances HER but inhibits ECO₂RR. The entire reversible process between the POM and heteropoly blue is summarized in Fig. 5(b). In a word, the reversible change between the POM and heteropoly blue is the key to balancing HER and ECO₂RR, and thus becomes an important factor for promoting the release of syngas from ECO₂RR.

The band structures of MInX₂ were first compared to demonstrate their electronic properties. As described in Fig. 6(a–c), the interaction between Cu and In d orbitals in CuInSe₂ results in a different band structure compared to AgInS₂ and CuInS₂. Specifically, CuInSe₂ exhibits metal-like features due to the overlap between the conduction and valence bands, while semiconductor property shown in AgInS₂ and CuInS₂ due to the appearance of band gaps. Consistent with the kinetic analysis in Section 3.3, the metal-like characteristic of CuInSe₂ would allow the passage of valence electrons, greatly facilitating charge

transfer and the electrochemical kinetic process. As is well known, the d-band center of a catalyst plays a critical role in the adsorption strength of reaction intermediates, which affects the reaction pathway and selectivity [18]. The d-band centers of MInX₂ relative to the Fermi level are summarized in Fig. 6(d). These d-band center positions relative to the Fermi level follow the order: CuInS₂ (-1.74 eV) > CuInSe₂ (-2.04 eV) > AgInS₂ (-2.92 eV). Therefore, as a key intermediate for the reaction route of CO₂ → CO, the adsorption strength of *CO would follow the following order: CuInS₂ > CuInSe₂ > AgInS₂ [52]. Therefore, *CO is adsorbed on the surface of CuInSe₂ with a mild adsorption strength. This result provided a support for the generation of CO and C₂ products. However, the weak adsorption of *CO on the surface of AgInS₂ only results in the evolution of CO. The strong adsorption of *CO on the surface of CuInS₂ results in the generation of C₂ products, which negatively affects the selectivity to the target product syngas. The slower reaction kinetics and higher reaction energy barrier of CuInS₂ explain its mediocre performance for the generation of both syngas and C₂ products.

The Gibbs free energy changes of MInX₂ during ECO₂RR were compared to further reveal the origin of their significantly different performance. As shown in Fig. 6(e), the RDS step of MInX₂ is *CO₂ → *COOH. For this step, the ΔG values of the three catalysts follow the order: CuInSe₂ (1.32 eV) < CuInS₂ (1.67 eV) < AgInS₂ (1.92 eV), indicating the enhanced ECO₂RR process achieved on CuInSe₂. For the *CO → CO step, the ΔG values follow the order: CuInS₂ (0.27 eV) > CuInSe₂ (0.25 eV) > AgInS₂ (0.07 eV), suggesting the mild adsorption strength for *CO adsorbed on the surface of CuInSe₂. This result was consistent with the above discussion of the d-band center, further elucidating the dual superiority of CuInSe₂ for synthesizing proportionally tunable syngas and C₂ products. Notably, the reaction energy barrier and ECO₂RR activity are related to the d-band center of MInX₂ relative to the Fermi level. Thus, a structure-function relationship can be established,

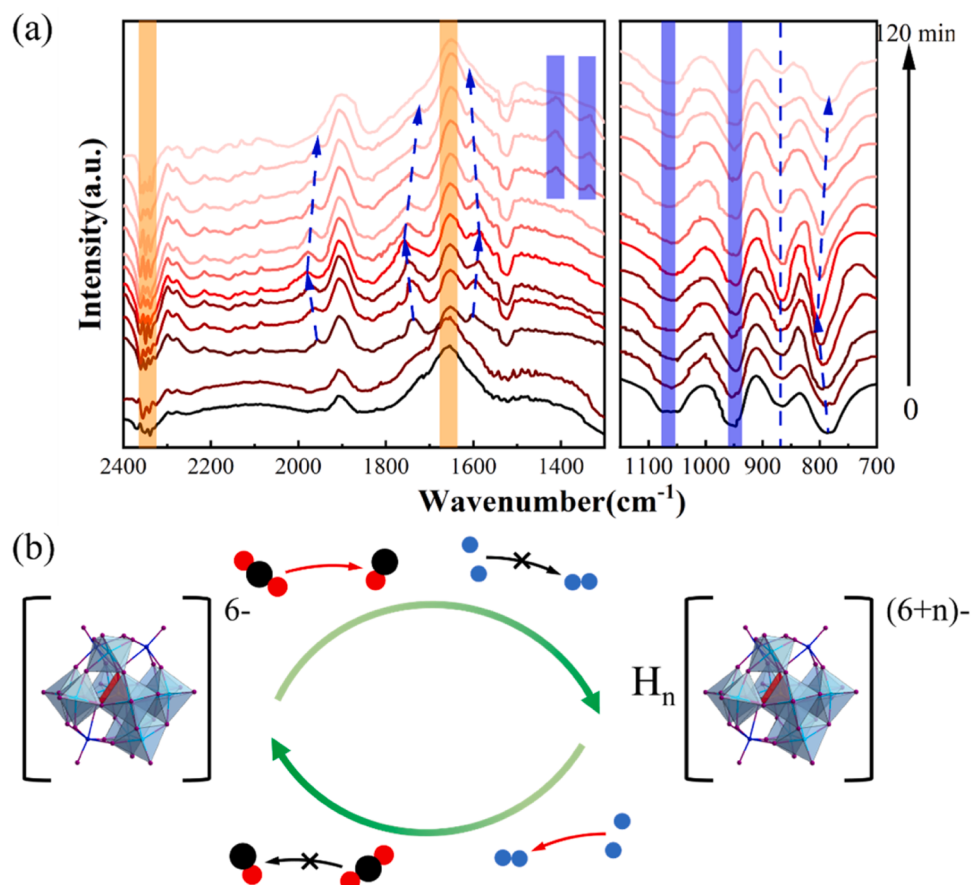


Fig. 5. (a) In-situ FTIR spectra of CuInSe₂ in POM medium at -0.5 V (vs. RHE) during 2 h ECO₂RR; (b) the reversible process between the POM and heteropoly blue.

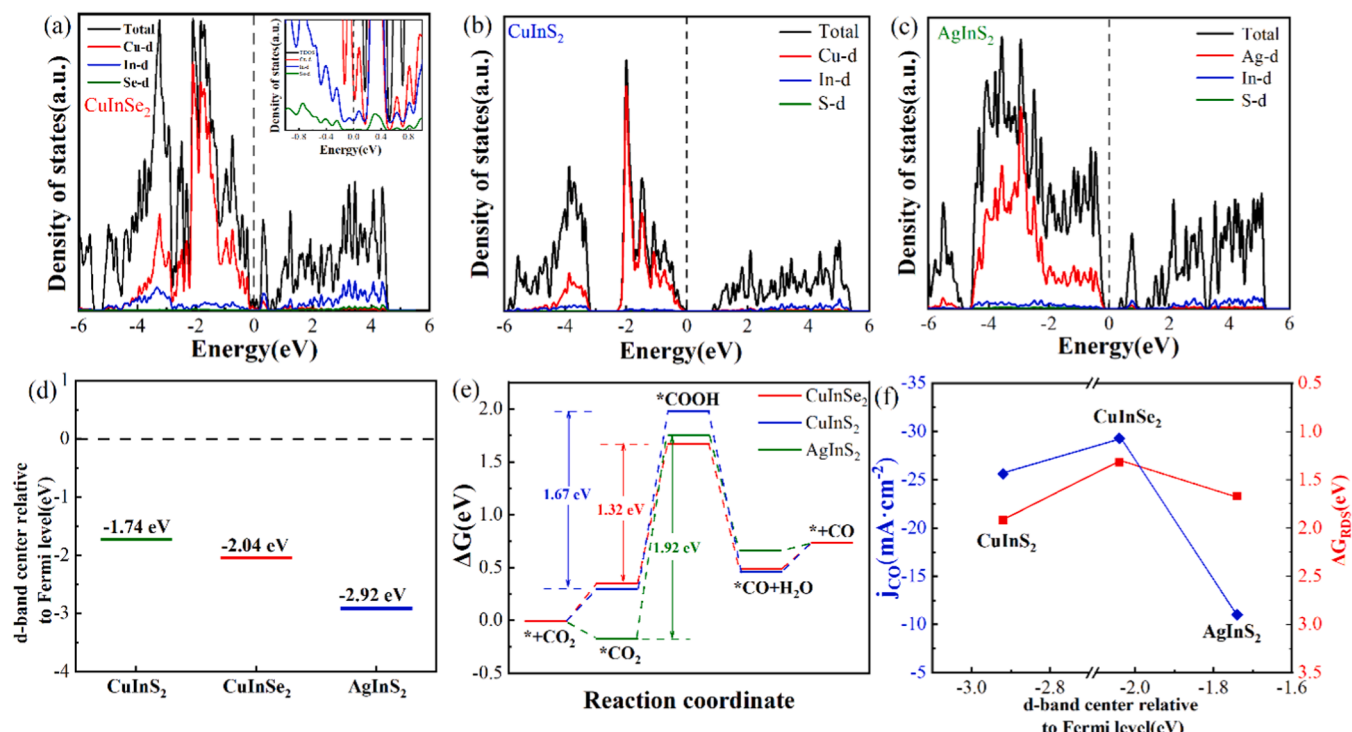


Fig. 6. The projected density of state (PDOS) of (a) CuInSe₂ (inset: Local magnification), (b) CuInS₂, (c) AgInS₂; (d) comparison of the d-band center relative to Fermi level; (e) Gibbs free energy changes of CO₂ → CO route on MInX₂; (f) the maximum value of j_{CO} and the ΔG_{RDS} relative to the d-band center position of MInX₂.

as shown in Fig. 6(f). CuInSe₂ exhibits a moderate d-band central energy level, lower reaction energy barrier, and significantly increased CO current density. Therefore, the bimetallic orbital interaction in CuInSe₂ facilitates an appropriate band structure, which optimizes the adsorption energy of intermediates and improves the activity of ECO₂RR. Based on the above results, the POM medium improves the reaction kinetics of ECO₂RR. The ECO₂RR performance of MInX₂ in the PV₃Mo₉ medium is more dependent on elemental composition than crystal structure. Thus, investigating the appropriate elemental composition may be highly significant for further improving the ECO₂RR performance.

Electrochemical reactions are jointly controlled by thermodynamics and kinetics [53]. As reported, the ΔG of HER in acidic environments is about 0 [54,55], suggesting that HER tends to be more controlled by kinetics. As a modulator of protons and electrons, different applied potentials can cause varying degrees of electron transfer behavior of PV₃Mo₉'s coordinating atoms, accompanied by the release of H⁺, thereby affecting the pH value of the electrolyte [20,21]. The local pH value at the electrode-electrolyte interface slightly increases because of H⁺ consumption. Therefore, the concentration gradient of H⁺ (i.e., the mass transfer driving force of HER) is controlled by the electron transfer behavior of PV₃Mo₉, which is influenced by the applied potential. In response, the occurrence of HER is affected by the kinetics regulated by the PV₃Mo₉ medium. The LSV and Tafel results confirm that the introduction of the PV₃Mo₉ medium improves the ECO₂RR kinetics. In terms of thermodynamics, as presented in Fig. 6(e), the overall $\Delta G > 0$. This indicates that ECO₂RR is mainly controlled by thermodynamics. Therefore, the mild regulation of the adsorption energy of reaction intermediates by the catalyst is the key to improving ECO₂RR performance. In summary, the dual effects of the PV₃Mo₉ medium and catalyst enable the composition of syngas to be proportionally tunable by changing the applied potential.

4. Conclusion

In summary, bimetallic chalcogenides with different elemental compositions were synthesized and combined with a PV₃Mo₉ medium to drive ECO₂RR, resulting in the generation of syngas with highly adjustable proportions at a lower onset potential (-0.1 V (vs. RHE)). The PV₃Mo₉ medium was more favorable for the reaction kinetics than a traditional aqueous solution, and this medium had a positive effect on reducing the onset potential. In addition, the metal-like characteristics of CuInSe₂ caused by its bimetallic orbital interaction and the mild adsorption of *CO on its surface were the main reasons for its high ECO₂RR activity in the POM medium. This work reveals the importance of the interaction between electrodes and electrolytes in electrochemical reactions to achieve high-performance ECO₂RR. Moreover, it further explores the potential of bimetallic chalcogenides in the preparation of syngas from ECO₂RR and provides a strategy for designing economically efficient ECO₂RR electrocatalysts with noble metal-like catalytic performance.

CRediT authorship contribution statement

Shumiao Li: Supervision, Software, Investigation, Conceptualization. **Min Yang:** Writing – review & editing, Supervision, Methodology, Conceptualization. **Li Zhou:** Supervision, Methodology, Investigation, Formal analysis. **Wenxue Tian:** Supervision, Software, Methodology, Investigation. **Wencong Sun:** Writing – original draft, Software, Methodology, Investigation, Conceptualization. **Chunxiang Li:** Writing – review & editing, Methodology, Investigation, Conceptualization.

Declaration of Competing Interest

The authors declare that they have no known competing financial interests or personal relationships that could have appeared to influence the work reported in this paper.

Data availability

Data will be made available on request.

Acknowledgements

The authors would like to thank Eceshi Lab (www.eceshi.com) for the TEM.

Appendix A. Supporting information

Supplementary data associated with this article can be found in the online version at doi:[10.1016/j.apcatb.2024.124206](https://doi.org/10.1016/j.apcatb.2024.124206).

References

- [1] W. Zhou, K. Cheng, J. Kang, C. Zhou, V. Subramanian, Q. Zhang, Y. Wang, New horizon in Cl chemistry: breaking the selectivity limitation in transformation of syngas and hydrogenation of CO₂ into hydrocarbon chemicals and fuels, *Chem. Soc. Rev.* 48 (2019) 3193–3228.
- [2] Y. Han, Z. Wang, X. Han, W. Fang, Y. Zhou, K. Lei, B. You, H.S. Park, B.Y. Xia, Selectively converting carbon dioxide to syngas over intermetallic AuCu catalysts, *ACS Sustain. Chem. Eng.* 9 (2021) 2609–2615.
- [3] R. He, A. Zhang, Y. Ding, T. Kong, Q. Xiao, H. Li, Y. Liu, J. Zeng, Achieving the widest range of syngas proportions at high current density over cadmium sulfoselenide nanorods in CO₂ electroreduction, *Adv. Mater.* 30 (2018) 1705872–1705878.
- [4] W. Ma, X. He, W. Wang, S. Xie, Q. Zhang, Y. Wang, Electrocatalytic reduction of CO₂ and CO to multi-carbon compounds over Cu-based catalysts, *Chem. Soc. Rev.* 50 (2021) 12897–12914.
- [5] L. Li, X. Li, Y. Sun, Y. Xie, Rational design of electrocatalytic carbon dioxide reduction for a zero-carbon network, *Chem. Soc. Rev.* 51 (2022) 1234–1252.
- [6] S. Agarwal, A.K. Singh, Electroreduction of CO₂ with tunable selectivity on au-pd bimetallic catalyst: a first principle study, *ACS Appl. Mater. Inter.* 14 (2022) 11313–11321.
- [7] H. Shi, H. Wang, Y. Zhou, J. Li, P. Zhai, X. Li, G.G. Gurzadyan, J. Hou, H. Yang, X. Guo, Atomically dispersed indium-copper dual-metal active sites promoting C-C coupling for CO₂ photoreduction to ethanol, *Angew. Chem. Int. Ed.* 61 (2022) 2022089.
- [8] Z. Zeng, L.Y. Gan, H.B. Yang, X. Su, J. Gao, W. Liu, H. Matsumoto, J. Gong, J. Zhang, W. Cai, Z. Zhang, Y. Yan, B. Liu, P. Chen, Orbital coupling of heterodiatomic nickel-iron site for bifunctional electrocatalysis of CO₂ reduction and oxygen evolution, *Nat. Commun.* 12 (2021) 4088–4098.
- [9] X. Sun, Y. Tuo, C. Ye, C. Chen, Q. Lu, G. Li, P. Jiang, S. Chen, P. Zhu, M. Ma, J. Zhang, J.H. Bitter, D. Wang, Y. Li, Phosphorus induced electron localization of single iron sites for boosted CO₂ electroreduction reaction, *Angew. Chem. Int. Ed.* 60 (2021) 23614–23618.
- [10] L. Jiao, J. Zhu, Y. Zhang, W. Yang, S. Zhou, A. Li, C. Xie, X. Zheng, W. Zhou, S.-H. Yu, H.-L. Jiang, Non-bonding interaction of neighboring Fe and Ni single-atom pairs on MOF-derived N-doped carbon for enhanced CO₂ electroreduction, *J. Am. Chem. Soc.* 143 (2021) 19417–19424.
- [11] C. Wang, Z. Lv, W. Yang, X. Feng, B. Wang, A rational design of functional porous frameworks for electrocatalytic CO₂ reduction reaction, *J. J. Chem. Soc. Rev.* 52 (2023) 1382–1427.
- [12] C. Li, Y. Ji, Y. Wang, C. Liu, Z. Chen, J. Tang, Y. Hong, X. Li, T. Zheng, Q. Jiang, C. Xia, Applications of metal-organic frameworks and their derivatives in electrochemical CO₂ reduction, *Nano-Micro Lett.* 15 (2023) 113–156.
- [13] J. Zheng, K. Lebedev, S. Wu, C. Huang, T.-S. Wu, Y. Li, P.-L. Ho, Y.-L. Soo, A. Kirkland, S.E. Tsang, High loading of transition metal single atoms on chalcogenide catalysts, *J. Am. Chem. Soc.* 143 (2021) 7979–7990.
- [14] J. Yin, J. Jin, H. Lin, Z. Yin, J. Li, M. Lu, L. Guo, P. Xi, Y. Tang, C.-H. Yan, Optimized metal halogenides for boosting water splitting, *Adv. Sci.* 7 (2020) 1903070–1903096.
- [15] W. Hu, D. Grandjean, J. Vaes, D. Pant, E. Janssens, Recent advances in copper chalcogenides for CO₂ electroreduction, *Phys. Chem. Chem. Phys.* 25 (2023) 30785–30799.
- [16] S. Liu, H. Tao, Q. Liu, Z. Xu, Q. Liu, J.-L. Luo, Rational design of silver sulfide nanowires for efficient CO₂ electroreduction in ionic liquid, *ACS Catal.* 8 (2018) 1469–1475.
- [17] J. Wang, X. Zheng, Y. Cao, L. Li, C. Zhong, Y. Deng, X. Han, W. Hu, Developing indium-based ternary spinel selenides for efficient solid flexible Zn-air batteries and water splitting, *ACS Appl. Mater. Inter.* 12 (2020) 8115–8123.
- [18] J. Wang, X. Zheng, G. Wang, Y. Cao, W. Ding, J. Zhang, H. Wu, J. Ding, H. Hu, X. Han, T. Ma, Y. Deng, W. Hu, Defective bimetallic selenides for selective CO₂ electroreduction to CO, *Adv. Mater.* 34 (2022) 2106354–2106361.
- [19] M.-L. Sun, Y.-R. Wang, W.-W. He, R.-L. Zhong, Q.-Z. Liu, S. Xu, J.-M. Xu, X.-L. Han, X. Ge, S.-L. Li, Y.-Q. Lan, A.M. Al-Enizi, A. Nafady, S. Ma, Efficient Electron transfer from electron-sponge polyoxometalate to single-metal site metal-organic frameworks for highly selective electroreduction of carbon dioxide, *Small* 17 (2021) 2100762–2100770.

- [20] Z. Lang, J. Miao, Y. Lan, J. Cheng, X. Xu, C. Cheng, Polyoxometalates as electron and proton reservoir assist electrochemical CO₂ reduction, *Apl. Mater.* 8 (2020) 120702–120714.
- [21] W. Sun, D. Yao, Y. Tai, L. Zhou, W. Tian, M. Yang, C. Li, Efficient electrocatalytic CO₂ reduction to ethanol through the proton coupled electron transfer process of PV_nMo_(12-n) (n=1, 2, 3) over indium electrode, *J. Colloid Interface Sci.* 650 (2023) 121–131.
- [22] P. Debergh, O. Gutierrez-Sanchez, M.N. Khan, Y.Y. Birdja, D. Pant, M. Bulut, The economics of electrochemical syngas production via direct air capture, *ACS Energy Lett.* (2023) 3398–3403.
- [23] W. Sun, Y. Tai, W. Tian, L. Zhou, C. Li, Electrochemical CO₂ reduction to ethanol: synergism of (n-Bu₄N)₃SVMo₁₁O₄₀ and an In catalyst, *Electrochim. Acta* 445 (2023) 142067–142074.
- [24] Q. Guo, S.J. Kim, M. Kar, W.N. Shafarman, R.W. Birkmire, E.A. Stach, R. Agrawal, H.W. Hillhouse, Development of CuInSe₂ nanocrystal and nanoring inks for low-cost solar cells, *Nano Lett.* 8 (2008) 2982–2987.
- [25] X. Lu, W. Che, X. Hu, Y. Wang, A. Zhang, F. Deng, S. Luo, D.D. Dionysiou, The facile fabrication of novel visible-light-driven Z-scheme CuInS₂/Bi₂WO₆ heterojunction with intimate interface contact by *in situ* hydrothermal growth strategy for extraordinary photocatalytic performance, *Chem. Eng. J.* 356 (2019) 819–829.
- [26] S. Liang, N. Altaf, L. Huang, Y. Gao, Q. Wang, Electrolytic cell design for electrochemical CO₂ reduction, *J. CO₂ Util.* 35 (2020) 90–105.
- [27] H. Shang, T. Wang, J. Pei, Z. Jiang, D. Zhou, Y. Wang, H. Li, J. Dong, Z. Zhuang, W. Chen, D. Wang, J. Zhang, Y. Li, Design of a single-atom indium⁵⁺-N₄ interface for efficient electroreduction of CO₂ to formate, *Angew. Chem. Int. Ed.* 59 (2020) 22465–22469.
- [28] Q. Wang, K. Liu, K. Hu, C. Cai, H. Li, H. Li, M. Herran, Y.-R. Lu, T.-S. Chan, C. Ma, J. Fu, S. Zhang, Y. Liang, E. Cortés, M. Liu, Attenuating metal-substrate conjugation in atomically dispersed nickel catalysts for electroreduction of CO₂ to CO, *Nat. Commun.* 13 (2022) 6082–6091.
- [29] W. Guo, X. Tan, J. Bi, L. Xu, D. Yang, C. Chen, Q. Zhu, J. Ma, A. Tayal, J. Ma, Y. Huang, X. Sun, S. Liu, B. Han, Atomic indium catalysts for switching CO₂ electroreduction products from formate to CO, 2021, *J. Am. Chem. Soc.* 143 (2021) 6877–6885.
- [30] P. Izadi, J. Song, C. Singh, D. Pant, F. Harnisch, Assessing the electrochemical CO₂ reduction reaction performance requires more than reporting coulombic efficiency, *Adv. Energ. Sust. Res.* (2024) 240031–240037.
- [31] G. Kresse, J. Furthmüller, Efficiency of ab-initio total energy calculations for metals and semiconductors using a plane-wave basis set, *Comp. Mater. Sci.* 6 (1996) 15–50.
- [32] P.E. Blöchl, Projector augmented-wave method, *Phys. Rev. B* 50 (1994) 17953–17979.
- [33] J.P. Perdew, J.A. Chevary, S.H. Vosko, K.A. Jackson, M.R. Pederson, D.J. Singh, C. Fiolhais, Atoms, molecules, solids, and surfaces: applications of the generalized gradient approximation for exchange and correlation, *Phys. Rev. B* 46 (1992) 6671–6687.
- [34] J.K. Norskov, J. Rossmeisl, A. Logadottir, L. Lindqvist, J.R. Kitchin, T. Bligaard, H. Jónsson, Origin of the overpotential for oxygen reduction at a fuel-cell cathode, *J. Phys. Chem. B* 108 (2004) 17886–17892.
- [35] H. Chen, J.-B. Yoo, Synthesis and characterization of CuInSe₂ nanoparticles via a solution method, *Mater. Res. Bull.* 47 (2012) 2730–2734.
- [36] Y. Liu, H. Wang, J. Zhao, Y. Liu, C. Liu, Ultra-deep desulfurization by reactive adsorption desulfurization on copper-based catalysts, *J. Energy Chem.* 29 (2019) 8–16.
- [37] L. Ding, N. Zhu, Y. Hu, Z. Chen, P. Song, T. Sheng, Z. Wu, Y. Xiong, Over 70% Faradaic efficiency for CO₂ electroreduction to ethanol enabled by potassium dopant-tuned interaction between copper sites and intermediates, *Angew. Chem. Int. Ed.* 61 (2022), 202209268–202209265.
- [38] H. Liu, Z. Jin, X. Wang, X. Zheng, Y. Wang, H. Du, L. Cui, Morphological growth and phase formation of CuInSe₂ nanocrystals by an ambient pressure polyol-based solution synthesis, *CrystEngComm* 14 (2012) 8186–8192.
- [39] S.D. Deshmukh, R.G. Ellis, D.S. Sutandar, D.J. Rokke, R. Agrawal, versatile colloidal syntheses of metal chalcogenide nanoparticles from elemental precursors using amine-thiol chemistry, *Chem. Mater.* 31 (2019) 9087–9097.
- [40] C. Yu, J.C. Yu, H. Wen, C. Zhang, A mild solvothermal route for preparation of cubic-like CuInS₂ crystals, *Mater. Lett.* 63 (2009) 1984–1986.
- [41] T. Xue, Y. Shi, J. Guo, M. Guo, Y. Yan, Preparation of AgInS₂ quantum dots and their application for Pb²⁺ detection based on fluorescence quenching effect, *Vacuum* 193 (2021) 110514–110524.
- [42] J. Du, Z.L. Lang, Y.Y. Ma, H.Q. Tan, B.L. Liu, Y.H. Wang, Z.H. Kang, Y.G. Li, Polyoxometalate-based electron transfer modulation for efficient electrocatalytic carbon dioxide reduction, *Chem. Sci.* 11 (2022) 3007–3015.
- [43] S. Zhang, P. Kang, S. Ubnoske, M.K. Brennaman, N. Song, R.L. House, J.T. Glass, T. J. Meyer, Polyethylenimine-enhanced electrocatalytic reduction of CO₂ to formate at nitrogen-doped carbon nanomaterials, *J. Am. Chem. Soc.* 136 (2014) 7845–7848.
- [44] C. Rincon, F.J. Ramirez, Lattice-vibrations of CuInSe₂ and CuGaSe₂ by Raman microspectrometry, *J. Appl. Phys.* 72 (1992) 4321–4324.
- [45] A. Predoeva, S. Damyanova, E.M. Gaigneaux, L. Petrov, The surface and catalytic properties of titania-supported mixed PMoV heteropoly compounds for total oxidation of chlorobenzene, *Appl. Catal. A-Gen.* 319 (2007) 14–24.
- [46] C. Yan, W. Luo, H. Yuan, G. Liu, R. Hao, N. Qin, Z. Wang, K. Liu, Z. Wang, D. Cui, Z. Hu, Y. Lan, Z. Lu, Stabilizing intermediates and optimizing reaction processes with N doping in Cu₂O for enhanced CO₂ electroreduction, *Appl. Catal. B-Environ.* 308 (2022) 121191–121199.
- [47] I.V. Chernyshova, P. Somasundaran, S. Ponnurangam, On the origin of the elusive first intermediate of CO₂ electroreduction, *P. Natl. Acad. Sci. USA* 115 (2018) E9261–E9270.
- [48] Y. Zhao, X. Chang, A.S. Malkani, X. Yang, L. Thompson, F. Jiao, B. Xu, Speciation of Cu surfaces during the electrochemical CO reduction reaction, *J. Am. Chem. Soc.* 142 (2020) 9735–9743.
- [49] Y. Katayama, F. Nattino, L. Giordano, J. Hwang, R.R. Rao, O. Andreussi, N. Marzari, Y. Shao-Horn, An *in situ* surface-enhanced infrared absorption spectroscopy study of electrochemical CO₂ reduction: selectivity dependence on surface C-bound and O-bound reaction intermediates, *J. Phys. Chem. C* 123 (2019) 5951–5963.
- [50] N. Mizuno, K. Katamura, Y. Yoneda, M. Misono, Catalysis by heteropoly compounds: V. The reduction mechanism of H₃PMo₁₂O₄₀, *J. Catal.* 83 (1983) 384–392.
- [51] C. Li, Y. Zhang, K. O'Halloran, J. Zhang, H. Ma, Electrochemical behavior of vanadium-substituted Keggin-type polyoxometalates in aqueous solution, *J. Appl. Electrochem.* 39 (2009) 421–427.
- [52] C. Zhu, A. Chen, J. Mao, G. Wu, S. Li, X. Dong, G. Li, Z. Jiang, Y. Song, W. Chen, W. Wei, Cu-Pd bimetallic gas diffusion electrodes for electrochemical reduction of CO₂ to C₂₊ products, *Small Struct.* 4 (2023) 2200328–2200336.
- [53] K.S. Exner, H. Over, Kinetics of electrocatalytic reactions from first-principles: a critical comparison with the ab initio thermodynamics approach, *Acc. Chem. Res.* 50 (2017) 1240–1247.
- [54] L. Guo, X. Bai, H. Xue, J. Sun, T. Song, S. Zhang, L. Qin, K. Huang, F. He, Q. Wang, MOF-derived hierarchical 3D bi-doped CoP nanoflower electrocatalyst for hydrogen evolution reaction in both acidic and alkaline media, *Chem. Commun.* 56 (2020) 7702–7705.
- [55] P. Qin, S. Yang, P. Zhan, M. Chu, G. Li, Z. Si, J. Shi, L. Lu, B. Han, T. Tan, Two-dimensional PdMo curved nanosheets for tunable CO₂ electrocatalytic reduction to syngas, *Cell Rep. Phys. Sci.* 2 (2021) 100619–100630.